nature energy

Article

https://doi.org/10.1038/s41560-024-01613-8

Diamine chelates for increased stability in mixed Sn–Pb and all-perovskite tandem solar cells

Received: 17 August 2023

Accepted: 23 July 2024

Published online: 15 August 2024

Check for updates

Chongwen Li[1,2,14], Lei Chen[3,14], Fangyuan Jiang[4,14], Zhaoning Song[3,14], Xiaoming Wang[3], Adam Balvanz[2], Esma Ugur[5], Yuan Liu[2], Cheng Liu[2], Aidan Maxwell[1], Hao Chen[1], Yanjiang Liu[1], Zaiwei Wang[1], Pan Xia[1], You Li[3], Sheng Fu[3], Nannan Sun[3], Corey R. Grice[3,6], Xuefei Wu[7], Zachary Fink[7,8], Qin Hu[7], Lewei Zeng[1], Euidae Jung[1], Junke Wang[1], So Min Park[1], Deying Luo[9], Cailing Chen[10], Jie Shen[10], Yu Han[10], Carlo Andrea Riccardo Perini[11], Juan-Pablo Correa-Baena[11], Zheng-Hong Lu[9], Thomas P. Russell[7,8,12], Stefaan De Wolf[5], Mercouri G. Kanatzidis[2], David S. Ginger[4], Bin Chen[1,2] ✉, Yanfa Yan[3] ✉ & Edward H. Sargent[1,2,13] ✉

Perovskite tandem solar cells show promising performance, but non-radiative recombination and its progressive worsening with time, especially in the mixed Sn–Pb low-bandgap layer, limit performance and stability. Here we find that mixed Sn–Pb perovskite thin films exhibit a compositional gradient, with an excess of Sn on the surface—and we show this gradient exacerbates oxidation and increases the recombination rate. We find that diamines preferentially chelate Sn atoms, removing them from the film surface and achieving a more balanced Sn:Pb stoichiometry, making the surface of the film resistive to the oxidation of Sn. The process forms an electrically resistive low-dimensional barrier layer, passivating defects and reducing interface recombination. Further improving the homogeneity of the barrier layer using 1,2-diaminopropane results in more uniform distribution and passivation. Tandems achieve a power conversion efficiency of 28.8%. Encapsulated tandems retain 90% of initial efficiency following 1,000 h of operating at the maximum power point under simulated one-sun illumination in air without cooling.

All-perovskite tandem solar cells have attracted attention for their rapid rise in power conversion efficiency (PCE) and their potential to surpass the detailed balance limit for single-junction solar cells[1–6]. Even with the impressive advances in recent years[7,8], there remains room to increase further their performance and achieve the durability required for commercial impact[9].

State-of-the-art all-perovskite tandems are built up from perovskite subcells based in the inverted p–i–n architecture[10–12]. However, a defective surface often emerges following annealing, leading to a high rate of surface recombination of charge carriers at the perovskite/electron transport layer interface[13–15]. This recombination is evidenced in a notable reduction in photoluminescence quantum yield (PLQY) upon contact with C_{60}[13], the electron transport layer for p–i–n subcells in tandems. Losses in device performance are particularly prominent in mixed tin (Sn)–lead (Pb) subcells, in which surface Sn^{2+} oxidation has been reported to induce deep trap states that increase surface

A full list of affiliations appears at the end of the paper. ✉e-mail: bin.chen@northwestern.edu; yanfa.yan@utoledo.edu; ted.sargent@northwestern.edu

https://doi.org/10.1038/s41560-024-01613-8

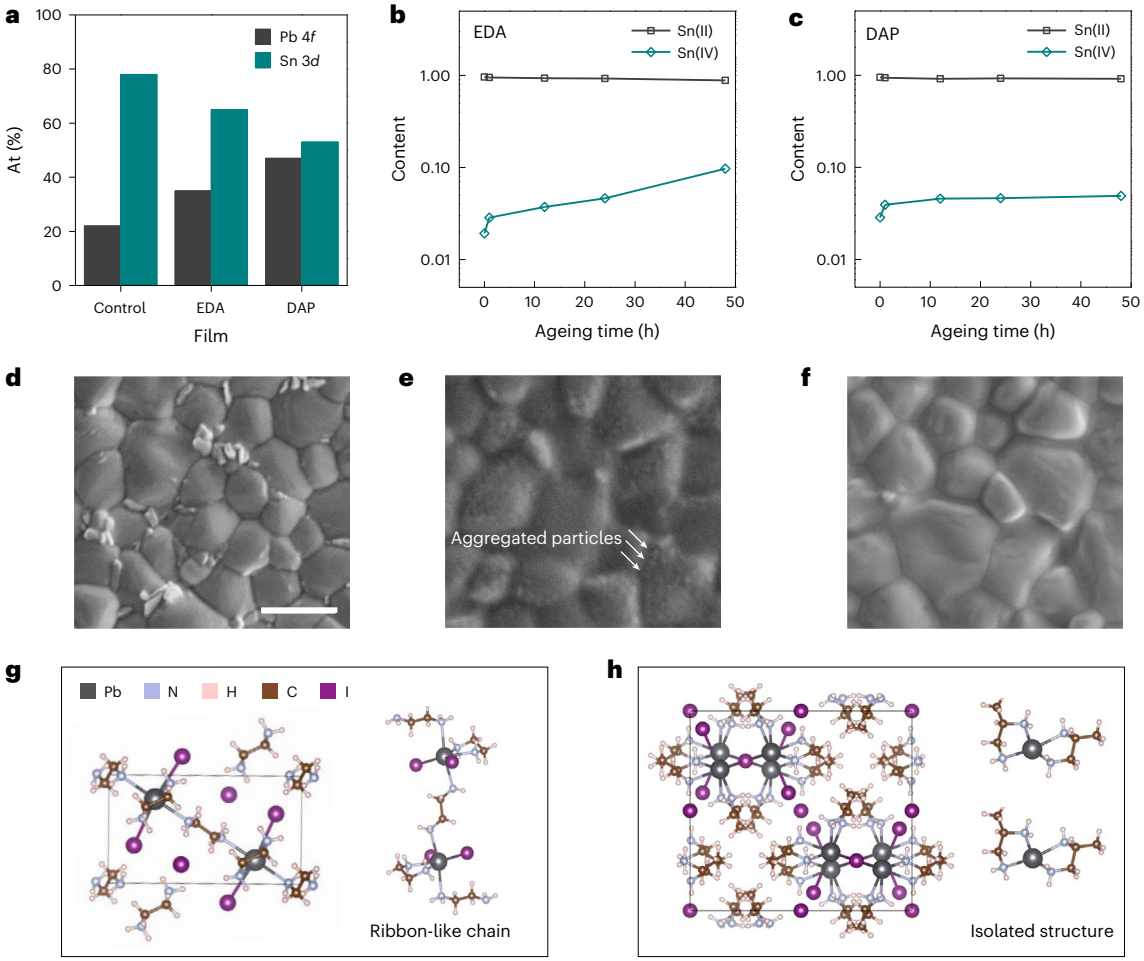

Fig. 1 | Oxidation inhabitation of mixed Sn–Pb films. a, Pb and Sn atomic (At) ratio of control, EDA- and DAP-treated mixed Sn–Pb perovskite thin films extracted from the surface XPS measurement. **b**,**c**, Sn (IV) content of mixed Sn–Pb films treated with EDA and DAP. **d**–**f**, SEM images of control, EDA- and DAP-treated mixed Sn–Pb perovskite thin films. The scale bar is 1 um. **g**,**h**, Crystal structure of $PbI_2(EDA)_2$ and $PbI_2(DAP)_2$ unit cells.

recombination and dark saturation current density by two orders of magnitude[16–18]. The defective surface contributes further to instability, limiting the operating stability of tandems[19].

Researchers have utilized additive engineering and post-treatment techniques to passivate surface defects, suppress Sn^{2+} oxidation and regulate crystallization dynamic in Sn-containing perovskite films[3,20–26]. These strategies have improved device performance in mixed Sn–Pb single-junction cells and tandems, but the susceptibility of Sn^{2+} at the surface to oxidation remains a challenge.

We find in the present study that diamines bind preferentially with Sn atoms, removing them from the film surface and balancing the Sn:Pb ratio, thereby improving resistance to oxidation. This process leads to the formation of diamine chelates that reduce interface recombination. We then strive to improve the homogeneity of the spatial distribution of the chelates via the use of 1,2-diaminopropane, this resulting in more uniform passivation. This enables a PCE of 23.9% for mixed Sn–Pb perovskite solar cells (PSCs). Mixed Sn–Pb PSCs (encapsulated) show improved operating stability in air, retaining 90% of initial PCE after 650 h of operation under maximum power point (MPP) tracking under simulated one-sun illumination. All-perovskite tandem solar cells made using a diamine-treated mixed Sn–Pb subcell and a 1.78 eV wide-bandgap subcell demonstrate a PCE of 28.8% and a T_{90} lifetime of 1,000 h.

Diamine chelates for the inhibition of oxidation

The formation of a Sn-rich compositional gradient at the surface could cause this interface to be especially prone to Sn^{2+} oxidation. We measured the Sn:Pb atomic ratio of $Cs_{0.05}FA_{0.7}MA_{0.25}Sn_{0.5}Pb_{0.5}I_3$ perovskite films using in-situ X-ray photoelectron spectroscopy (XPS) and saw an Sn-rich compositional gradient with the Sn:Pb ratio equal to ~4:1 at the surface (Supplementary Figs. 1 and 2). We aged a mixed Sn–Pb film in air for 1 h and found that ~35% of Sn is in the desired Sn^{2+} oxidation state, whereas the remaining ~65% is in the undesired Sn^{4+} oxidation state (Supplementary Fig. 3) known to produce p-type self-doping and an increased density of defect states[16,27,28].

We then contemplated a means to preserve the Sn:Pb ratio at the surface compared with in bulk. Diamines are bidentate chelating ligands possessing strong coordination with Pb[29]. Because Sn has stronger Lewis acidity than Pb, we sought to chelate Sn/Pb atoms in mixed Sn–Pb perovskites using diamines and selectively remove the excess Sn at the surface (Supplementary Table 1).

We examined chelation using ethylenediamine (EDA), the liquid diamine that shows the most simplicity in molecular structure (Supplementary Fig. 4a). We prepared a mixed Sn–Pb film post treated with EDA and evaluated its ability to remove residual Sn using XPS. We observed a slight decrease in the Sn:Pb ratio from ~4:1 in the pristine mixed Sn–Pb film (referred to hereafter as control) to ~2:1 in the film treated with EDA (Supplementary Fig. 5 and Fig. 1a), indicating the removal of surface residual Sn with EDA.

We evaluated the ability of diamine chelation to improve the oxidation resistance of mixed Sn–Pb thin films. XPS analysis reveals that in the control film, Sn^{4+} rapidly reaches ~65% after storing for 1 h and then stabilizes at ~80% thereafter (Supplementary Fig. 3). EDA suppresses

https://doi.org/10.1038/s41560-024-01613-8

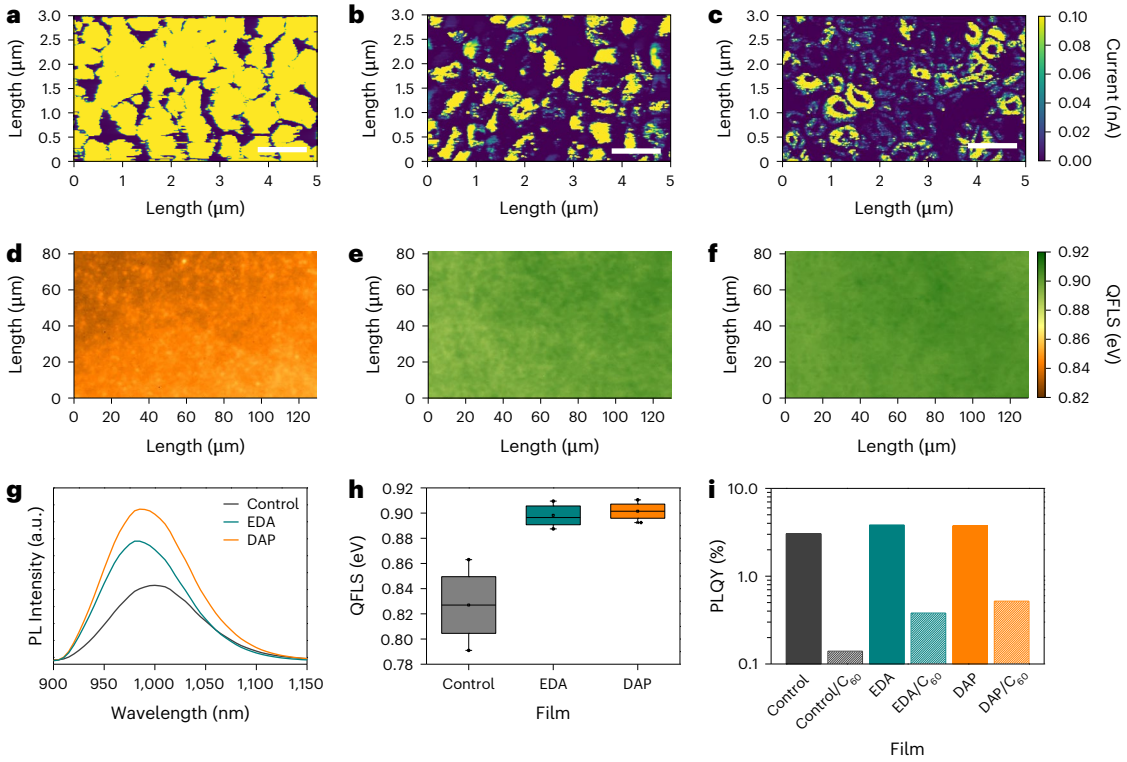

Fig. 2 | Surface passivation of mixed Sn–Pb films. a–**c**, cAFM images of control, EDA- and DAP-treated mixed Sn–Pb perovskite thin films. The scale bar is 1 um. **d**–**f**, QFLS maps of control, EDA- and DAP-treated mixed Sn–Pb perovskite thin films. **g**, PL spectra of control, EDA- and DAP-treated mixed Sn–Pb perovskite thin films. **h**, QFLS statistic of the thin films over the surface of the samples. Nineteen pixels of each set of samples were measured. The boxes indicate 25th (upper quartile) to 75th (lower quartile) percentiles. The whiskers show the range to the upper and lower extremes. The small squares and solid lines in the boxes represent the mean points and median lines. **i**, PLQY of thin films before and after C_{60} deposition.

Sn oxidation, with only ~2% of Sn in its Sn^{4+} oxidation state after 1 h (Supplementary Fig. 6). However, in the EDA-treated film, Sn^{4+} gradually increases to ~10% after 48 h (Fig. 1b), which may indicate undesirable surface treatment that reduces long-term resistance to oxidation.

We used scanning electron microscopy (SEM) to track surface morphological changes. Control films show crystalline grain domains with bright crystals, probably SnF_2/SnI_2 residues at grain boundaries (Fig. 1d)[30,31]. In contrast, films treated with EDA exhibit a distinct amorphous morphology, with small particles that are probably chelates randomly aggregated on grains (Fig. 1e). The stability of chelates was assessed by preparing films of SnI_2 and SnI_2-EDA for XPS analysis. We observed reduced atomic ratios of both Sn and I oxidation states (Supplementary Fig. 7), indicating improved stability against atmospheric oxygen. We offer that the inhomogeneous/aggregated EDA chelates on grains may reduce the ability to provide film-wide resistance to oxidation.

We extended our studies of diamine chelation to analogous diamines but having longer chain lengths: 1,4-diaminobutane and 1,5-diaminopentane (Supplementary Fig. 4). We saw using XPS reduced surface Sn content after diamine chelation (Supplementary Fig. 8). These diamines also contribute to suppressed Sn oxidation, while exhibiting gradual oxidation over time (Supplementary Figs. 9 and 10), which may result from undesirable surface chelate distribution (Supplementary Fig. 11).

To understand the structure of chelates and the design principles underpinning the use of functional diamines, we grew single crystals to assess local atomic arrangement of the chelates[32]. We attempted the synthesis of EDA-SnI_2, but the compound consisted of insoluble fine powders with no discernible diffraction pattern, possibly due to the oxidation of Sn during synthesis. Because Pb- and Sn-based single crystals are isostructural[33,34], we predict that SnI_2-EDA and PbI_2-EDA crystals are also isostructural. We prepared $PbI_2(EDA)_2$ crystals and found that they exhibit a polymeric chain structure (Fig. 1g), where one EDA molecule chelates one Pb atom, whereas the other EDA is shared by the adjacent two Pb atoms (Supplementary Fig. 12, Supplementary Note 1 and Supplementary Tables 2–4). The ribbon-like structure tends to aggregate and localize on perovskite grains, offering an account of the small particles seen in SEM (Fig. 1e) and accounting for the progressive oxidation of Sn (Fig. 1b).

To overcome this issue, we moved to using a methyl group attached to one of the nitrogen atoms in EDA (Supplementary Fig. 4), our goal to introduce steric hindrance to hinder the formation of the chain structure. This diamine, 1,2-diaminopropane (DAP), in a given $PbI_2(DAP)_2$ unit cell chelates the same Pb atom, resulting in an isolated non-perovskite structure (Fig. 1h and Supplementary Fig. 13). These isolated DAP chelates are not constrained by the rigid chain-like crystal lattice and are thus able to distribute more evenly on grains with the absence of aggregated particles seen in the film treated with EDA (Fig. 1f). The improvement in the homogeneity of chelate distribution enables mixed Sn–Pb films with a more balanced Sn:Pb ratio of ~1:1 (Fig. 1a) and much improved long-term resistance to oxidation, stabilizing Sn^{4+} content at ~5% after 12 h and thereafter (Fig. 1c and Supplementary Fig. 14).

Surface reconstruction and passivation

We turned to study in more detail on the diamine treatment reconstructs the Sn–Pb perovskite surface. XPS shows that the Sn- and Pb-associated peaks shift to lower energies following diamine treatment (Supplementary Fig. 15), whereas carbon remains unchanged. This suggests the transfer of electrons from the N of the diamines to Sn and Pb and the chelation of the metal atoms. Using grazing-incidence wide-angle X-ray scattering (GIWAXS), we observed q_r peaks at 0.78 and 0.64 $Å^{-1}$ with the EDA-treated sample and 0.70 and 0.45 $Å^{-1}$ for the DAP-treated sample,

https://doi.org/10.1038/s41560-024-01613-8

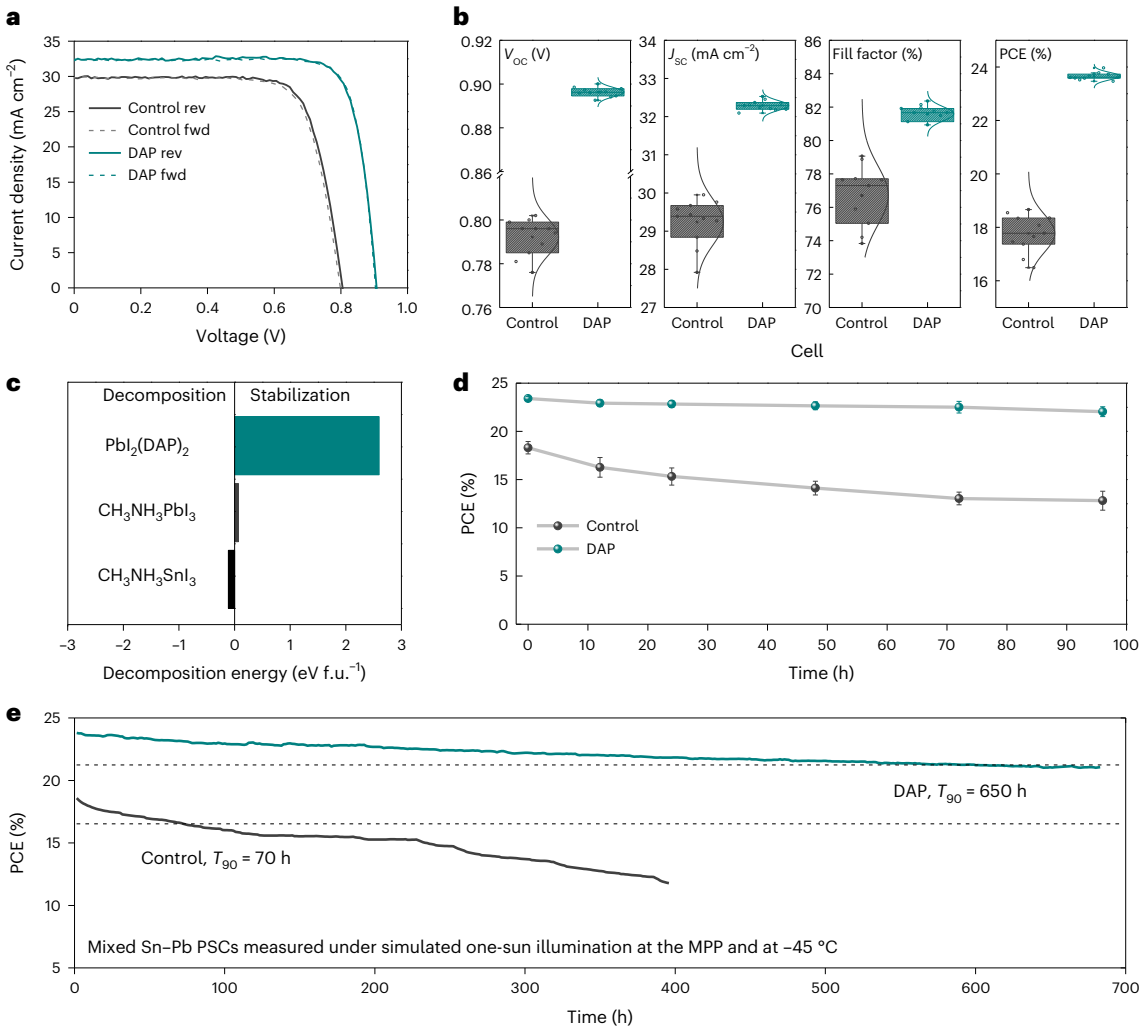

Fig. 3 | Performance and stability of mixed Sn–Pb PSCs. a, *J*–*V* curves of control and DAP-treated mixed Sn–Pb cells measured under reverse (rev) and forward (fwd) scans. **b**, PCE statistics of control and DAP-treated mixed Sn–Pb cells. 11 cells of each set of solar cells were measured. The boxes indicate 25th (upper quartile) to 75th (lower quartile) percentiles. The whiskers show the range to the upper and lower extremes. The small squares, solid lines and coloured circles in the boxes represent the mean points, median lines, and statistical data points. The break in the 'V_{OC}' y-axis is to better show the difference between the Control and DAP cells. **c**, Decomposition energies per formula unit (denoted as eV f.u.−1) of $PbI_2(DAP)_2$ unit cells, $CH_3NH_3PbI_3$ and $CH_3NH_3SnI_3$. **d**, Thermal stability of control and DAP-treated PSCs. The filled circles and error bars represent the mean values and standard deviations of 5 cells measured at each condition. **e**, MPP stability results of control and DAP-treated PSCs measured under a white LED solar simulator with simulated one-sun illumination.

indicating the formation of ribbon-like and isolated chelate structures in EDA and DAP samples (Supplementary Fig. 16 and Supplementary Note 2). The thickness of the chelates was further estimated using sputtering XPS to be in the range ~ 5–7 nm (Supplementary Fig. 17 and Supplementary Note 3). We speculate these layers could involve a mixture of diamine-metal chelation products and low-dimensional phases resulting from the reaction of diamines with formamidinium iodide (FAI)[35,36].

Next we investigated how reconstruction affects the surface properties. We used conductive atomic force microscopy (cAFM) to investigate surface passivation and local resistance. The domain interiors of control films exhibited >0.1 nA current at 1.5 V bias, whereas the interfaces between domains show much lower conductance (Fig. 2a). After diamine treatment, the entire film surface becomes less-conductive (Fig. 2b,c), resulting from the reduced electronic dimensionality of chelates and possible products of reactions between the diamines and FAI[35,36].

We analysed the map of current extraction with the aid of cAFM. A typical control sample shows bimodal current distribution (Supplementary Fig. 18a), with ~30% of pixels showing a current <0.1 nA and ~60% of pixels having a current >1 nA, corresponding to the non-conductive interfaces and conductive domains. In the EDA-treated sample, we observed a broader current distribution, but with only 5% of pixels reaching a current >1 nA (Supplementary Fig. 18b,c). This decrease in surface conductivity, along with the remaining conductive regions, correlates with the above-noted aggregation on grains, the result of which is that some areas remained untreated. DAP-treated samples have a narrower current distribution, with almost no pixels having current above 1 nA (Supplementary Fig. 18d), showing more uniform chelate distribution and passivation.

A homogenized spatial conductivity distribution was observed after the deposition of the C_{60} layer (Supplementary Fig. 19), indicating that the modest percentage of conductive regions on the DAP-treated perovskite surface allows efficient current extraction through the conductive regions without sacrificing device performance. The lower bound of the conductive pixels was suggested to be ~10% of the perovskite surface before negatively impacting the solar cell performance (Supplementary Fig. 20 and Supplementary Note 4).

In photoluminescence (PL) characterization, diamine-treated films exhibit blue-shifted emission peaks and increased peak intensities compared with controls (Supplementary Fig. 21 and Fig. 2g). The surface distribution of quasi-Fermi level splitting (QFLS) of the samples

https://doi.org/10.1038/s41560-024-01613-8

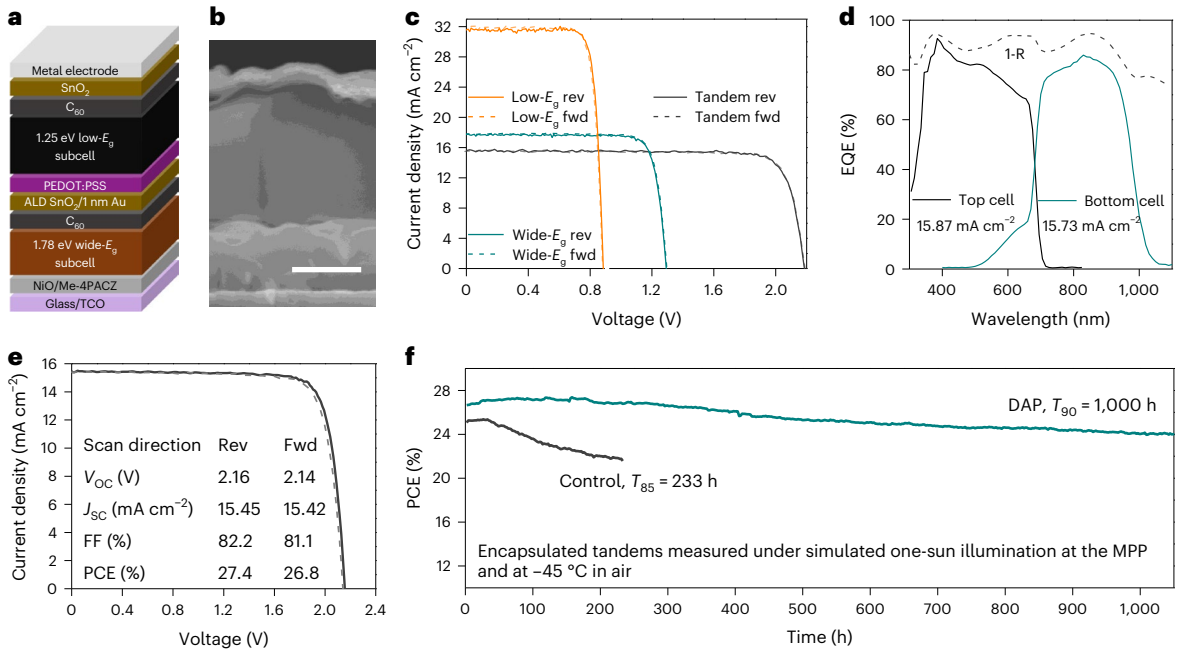

Fig. 4 | Tandem device performance and stability. a,**b**, Device architecture and a cross-sectional SEM image of a tandem. The scale bar is 500 nm. The composition of the wide-bandgap (E_g) subcell is $FA_{0.8}Cs_{0.2}Pb(I_{0.63}Br_{0.37})_3$. **c**, *J*–*V* curves of low-bandgap, wide-bandgap and tandem cells. **d**, EQE curves and the reflection loss (denoted as 1-R) of a tandem. **e**, Certified *J*–*V* curves of a tandem. **f**, MPPT results of control and DAP-treated tandems measured under a white LED solar simulator with simulated one-sun illumination. Credit: **e**, JET.

are shown in QFLS maps in Fig. 2d–f. The values are 0.827 ± 0.022 eV, 0.898 ± 0.008 eV and 0.902 ± 0.005 eV for control, EDA- and DAP-treated films, respectively (Fig. 2h). The PL decay of the mixed Sn–Pb films was measured using time-correlated single photon counting (Supplementary Fig. 22). For the sample stack of glass/perovskite, the carrier lifetime increased from 1.37 µs for the control sample to 3.16 and 3.43 µs for the EDA- and DAP-treated films, and for the sample stack of glass/perovskite/C60, the carrier lifetime decreased from 113.8 ns to 85.1 and 55.8 ns, which are indicative of reduced surface recombination and accelerated charge extraction at the perovskite/C_{60} interface.

PLQY measurements on half cells with a C_{60} layer we used to assess ability to reduce interfacial recombination. EDA-treated films showed a factor of three improvement in PLQY (Fig. 2i), with a factor of four improvement in the case of DAP. This increase in the half stacks is consistent with the formation of electrically resistive chemical barrier layers, which could be beneficial for electronically decoupling the bulk perovskite from the fullerene layer as has been shown to improve PLQY and open circuit voltage (V_{OC}) for other insulating layers[37].

Stability of mixed Sn–Pb perovskite solar cells

We fabricated 1.25 eV $Cs_{0.05}FA_{0.7}MA_{0.25}Sn_{0.5}Pb_{0.5}I_3$ cells with the architecture shown in Supplementary Fig. 23. The optimal concentration of EDA and DAP in chlorobenzene was found to be 0.05 µl ml^{-1} and 0.25 µl ml^{-1} (Supplementary Fig. 24). The band alignment was reported by the ultraviolet photoelectron spectroscopy (Supplementary Fig. 25). After DAP treatment, the chelate barrier layer induces a more *n*-type doped perovskite film surface with the work function upshifted from -4.81 eV to -4.45 eV, and this we expect should facilitate electron extraction and reduce interface non-radiative recombination, resulting in improved V_{OC}. Figure 3a and Supplementary Fig. 26 compare the current density–voltage (*J*–*V*) curves of the highest-performing cells (details in Supplementary Table 5). The V_{OC} increased from 0.81 V for the control device to 0.90 V for the DAP-treated device, contributing to an increased PCE of 23.90% with improved reproducibility (Fig. 3a,b and Supplementary Fig. 27). The *J*–*V* current density of 32.5 mA cm^{-2} agrees with the value of 32.0 mA cm^{-2} measured from integrated external quantum efficiency (EQE; Supplementary Fig. 28). The improved performance of DAP-treated devices is consistent with reduced interface recombination at the perovskite/C_{60} interface (Supplementary Figs. 21 and 22 and Fig. 2g,i).

We performed stability tests on the control and DAP-treated mixed Sn–Pb PSCs. We used 1,3-Bis(diphenylphosphino)propane and Cr/Cu electrodes for interface toughness and to reduce electrode corrosion[38]. The effect of DAP barrier layer in improving resistance against oxidation was first tested by ageing unencapsulated solar cells in ambient air: the DAP-treated Sn–Pb cell retained ~90% of its initial PCE after 48 h in ambient air with a relative humidity of approximately 25%, whereas the control PCE dropped to < 20% of its initial value (Supplementary Fig. 29).

We then performed accelerated thermal stress tests at 85 °C on a hotplate in the glovebox and measured PCEs periodically to test thermal durability. We tested 5 pixels at each condition, and the average PCE of control devices diminished to <70% of their initial value following 96 h; whereas it retained ~90% in the DAP-treated devices (Fig. 3d). The decomposition of surface species has been reported to limit thermal stability of mixed Sn–Pb films[10]. We calculated decomposition energy—that required to decompose a compound into its precursors. The decomposition energies of $PbI_2(DAP)_2$ was found to be 2.6 eV per formula unit (f.u.$^{-1}$), higher than the −0.111 and 0.070 eV f.u.$^{-1}$ reported previously for $CH_3NH_3PbI_3$ and $CH_3NH_3SnI_3$ (Fig. 3c and Supplementary Table 6)[39,40], suggestive of increased stability of chelates. As these stable chelates are evenly distributed on the film surface, we propose that they cover and protect the surface against thermal stress.

We further tested the operating stability of solar cells under continuous 1-sun illumination in an N_2 environment at a temperature of ~45 °C. The PCE of a control mixed Sn–Pb PSC decreased to <90% of its initial PCE after 90 h, whereas a DAP-treated PSC showed much improved stability under light, retaining 90% of its initial PCE after 650 h (Fig. 3e). Further actions, such as replacing acidic PEDOT:PSS, will be needed to enable more stable mixed Sn–Pb PSCs under rigorous thermal and light stresses.

Tandem performance and stability

We fabricated tandems (Fig. 4a–c) that achieved champion 28.83 (28.42)% with a V_{OC} of 2.18 (2.19) V, along with a J_{SC} of 15.57 (15.59) mA cm^{-2}

and FF of 84.8 (83.4)% under reverse (forward) scan (Supplementary Table 7). Stabilized power output reached 28.5% in ten tandems (Supplementary Fig. 30) with current densities consistent with EQEs (Fig. 4d). *J*–*V* scans from Japan electrical safety and environment technology laboratories (JET) delivered a PCE of 27.4% (Fig. 4e, Supplementary Fig. 31 and Supplementary Note 5). One cm^2 tandems achieved a PCE of 27.53 (27.41)% with V_{OC} of 2.18 (2.18) V, J_{SC} of 15.82 (15.71) mA cm^{-2} and FF of 79.8 (79.9)% (Supplementary Fig. 32).

We tested the stability using MPP tracking in air and under simulated 1-sun illumination (Fig. 4f). An encapsulated tandem retained 90% (T_{90}) of its original PCE after 1,000 h continuous operation in ambient air without cooling, surpassing the 233 h of the control device. We compare our devices with the highest-performing and most-stable previously published all-perovskite tandems in Supplementary Table 8.

Methods

Materials

Formamidinium iodide (FAI, 99.999%), methylammonium iodide (MAI, 99.999%) and lead iodide (PbI_2, 99.999%) were purchased from Advanced Election Technology Co. Tin iodide (SnI_2, 99.99%), tin fluoride (SnF_2, 99%), caesium iodide (CsI, 99.999%), caesium bromide (CsBr, 99.999%) and 1,3-Bis(diphenylphosphino)propane (DPPP, 97%) were purchased from Sigma-Aldrich. C_{60}, bathocuproine (BCP), [4-(3,6-Dimethyl-9H-carbazol-9-yl)butyl]phosphonic acid (Me-4PACz, >99.0%), guanidinium thiocyanate (GuaSCN, ≥99%) and 1,3-propane-diammonium iodide ($PDAI_2$) were purchased from Xi'an Polymer Light Technology. Formamidinium bromide (FABr, >99.99%) and 4-fluoro-phenethylammonium bromide (4F-PEABr) were purchased from Greatcell Solar Materials.

Ethylenediamine (EDA, ≥99%), 1,2-diaminopropane (DAP, 99%), 1,4-diaminobutane (99%), 1,5-diaminopentane (95%), dimethylsulfoxide (DMSO, ≥99.9%), anisole (99.7%), chlorobenzene (CB, ≥99.5%), isopropanol (IPA, ≥99.5%), toluene (99.8%), dimethylformamide (DMF, ≥99.5%) were purchased from Sigma-Aldrich. Nickel oxide (NiO_x) nanoparticle solution was purchased from Avantama. Poly(3,4-ethylenedioxythiophene) polystyrene sulfonate solution (PEDOT: PSS, Al-4083) was purchased from Ossila.

Tetrakis(dimethylamino) tin (iv) (99.99%-Sn, 50-1815 Tin) was purchased from Strem Chemicals. Commercial indium tin oxide (ITO) glasses (15 Ω per square) with 25 mm × 25 mm dimension were purchased from Suzhou ShangYang Solar Technology Co. Copper, silver and gold were purchased from Kurt J. Lesker. UV-curable epoxy was purchased from Luminescence technology corp.

Preparation of precursor solutions

Low-bandgap perovskite solution. Low-bandgap perovskite precursor solution (1.8 M, $Cs_{0.05}FA_{0.7}MA_{0.25}Sn_{0.5}Pb_{0.5}I_3$) was prepared by dissolving CsI (23.4 mg), FAI (216.7 mg), MAI (71.55 mg), SnI_2 (335.3 mg) and PbI_2 (414.9 mg) in mixed solvent of DMF (750 µl) and DMSO (250 µl). GuaSCN (4 mg), SnF_2 (14.1 mg) and 4F-PEABr (1.5 mg) were added to the precursor solution as additives.

Wide-bandgap perovskite solution. Wide-bandgap perovskite precursor solution (1.2 M, $FA_{0.8}Cs_{0.2}Pb(I_{0.63}Br_{0.37})_3$) was prepared by dissolving CsI (34.3 mg), CsBr (18.7 mg), FAI (91 mg), FABr (44 mg), $PbBr_2$ (143.3 mg) and PbI_2 (327.1 mg) in mixed solvent of DMF (800 µl) and DMSO (200 µl).

Post-treatment solutions. EDA and DAP were dissolved in CB with varying concentrations (EDA: 0.025 µl ml^{-1}, 0.05 µl ml^{-1}, 0.075 µl ml^{-1} and 0.1 µl ml^{-1}; DAP: 0.2 µl ml^{-1}, 0.25 µl ml^{-1}, 0.3 µl ml^{-1} and 0.5 µl ml^{-1}). One mg ml^{-1} $PDAI_2$ was dissolved in mixed solvent of IPA and CB with the volume ratio of 2:1.

Hole transport material solutions. NiO_x nanoparticle solution was diluted to 0.025 wt% in ethanol. Me-4PACZ was dissolved in ethanol with the concentration of 0.3 mg ml^{-1}.

All-perovskite precursor solutions were dissolved using a magnetic stir bar at room temperature without annealing. Before using, perovskite precursor solutions were filtered by a 0.22-µm polytetrafluoroethylene membrane.

Preparation of solar cells

The prepatterned ITO substrates were cleaned by ultrasonication in diluted Micro-90 detergent, deionized water, acetone and isopropanol for 15 min, respectively. Before making thin films, the ITO substrates were cleaned using UV–ozone cleaner for 20 min. The temperature of the hotplates used for annealing were calibrated using a thermocouple before serving.

Low-bandgap perovskite solar cells. Low-bandgap perovskite solar cells have a device configuration of glass/ITO/PEDOT:PSS/$Cs_{0.05}FA_{0.7}MA_{0.25}Sn_{0.5}Pb_{0.5}I_3/C_{60}$/ALD-$SnO_2$/Ag, where ITO, PEDOT:PSS and ALD stand for indium tin oxide, poly(3,4-ethylenedioxythiophene) polystyrene sulfonate and atomic layer deposition, respectively. PEDOT:PSS solution was spin coated on cleaned ITO substrates at 4,000 rpm for 25 s and dried at 150 °C for 20 min. Perovskite precursor solutions (60 ul) were then spin coated on the ITO/PEDOT:PSS substrates in the glovebox at 1,000 rpm for 10 s and then 3,800 rpm for 40 s. Toluene (350 µl) was applied drop-wise at 30 s onto the spinning substrate during the spin coating. The perovskite films were annealed at 100 °C for 10 min for crystallization. Sixty µl of diamine solution was then applied on the annealed films at 3,000 rpm for 25 s, followed by an annealing process at 100 °C for 5 min. The perovskite films were then transferred to a thermal evaporation chamber for the C_{60} (25 nm) deposition at the rate of 0.2 Å s^{-1}, followed by the SnO_2 (5 nm) deposition in an ALD chamber. Ag (80 nm) or Cu (80 nm)/Cr (5 nm) electrodes were deposited in a thermal evaporation chamber for efficiency or stability tests.

Wide-bandgap perovskite solar cells and all-perovskite tandem solar cells. NiO_x and Me-4PACZ solutions were spin coated on cleaned ITO substrates at 4,000 rpm for 25 s, subsequently, and then annealed on a 100 °C hotplates for 10 min. DPPP solution (1 mg ml^{-1} in DMF) was spin coated on the ITO/NiO_x/Me-4PACZ substrates at 5,000 rpm for 25 s and then annealed at 100 °C for 2 min. Perovskite precursor solutions (60 µl) were then spin coated on the substrates in the glovebox at 3,700 rpm for 40 s. Anisole (150 µl) was applied drop-wise at 15 s onto the spinning substrate during the spin coating. The perovskite films were annealed at 110 °C for 15 min for crystallization. The deposition of electron transport layers and electrodes followed the same procedures for low-bandgap perovskite solar cells. For assembling all-perovskite tandem solar cells, we deposited 1 nm Au on the SnO_2 layer on wide-bandgap subcells as the recombination layer and then deposited the low-bandgap subcells following the same procedure as discussed above. Finally, Ag (80 nm) or Cu (80 nm)/Cr (5 nm) electrodes were deposited in a thermal evaporation chamber for efficiency or stability tests. The solar cells were encapsulated with cover glasses and UV-curable epoxy before efficiency and stability tests.

Solar cell characterizations

The *J*–*V* characteristics were measured using a Keithley 2400 source meter under illumination from a solar simulator (Newport, Class AAA) with the irradiation intensity of 100 mW cm^{-2} AM 1.5 G (checked with a calibrated reference Si solar cell from Newport). *J*–*V* curves measurement with a scanning rate of 100 mV s^{-1} (voltage step of 10 mV and delay time of 100 ms) and stabilized power output (SPO) measurement were conducted in nitrogen atmosphere without cooling. The aperture shade mask (0.049 cm^2 for small-area and 1.05 cm^2 for large-area devices) determined the active area of the solar cell. Maximum power point (MPP) tracking measurements were conducted using a Candlelight stability test station in the air and under a white light-emitting diode (LED) solar

simulator (Supplementary Fig. 33) with simulated one-sun illumination. The humidity of the measurement environment ranged from 40 to 60%. The curves drawn on top of efficiency and stability data in Fig. 3d and Supplementary Figs. 20d and 29 were guides to the eye.

A quantum efficiency system (PV Measurements Inc., model IVQE8-C QE system) was used to measure the quantum efficiency of the PSCs. A standard Si solar cell was used as the reference for calibration. For EQEs of low-bandgap and wide-bandgap subcells, we used 530 nm and 705 nm lasers to saturate the other junction during EQE measurement, respectively.

DFT calculations

Density functional theory calculations were performed using the VASP code[41,42] with projector augmented-wave potentials. A plane-wave energy cut-off of 600 eV and Γ centred $4 \times 4 \times 2$ $(PbI_2(EDA)_2)$ and $2 \times 2 \times 2$ $(PbI_2(DAP)_2)$ k meshes were used. The exchange–correlation interactions were treated with the generalized gradient approximation of the Perdew–Burke–Ernzerhof parametrization. Grimme's D3 correction were also included to deal with the van der Waals interactions. Both the lattice and atomic positions are relaxed with force tolerance of 0.01 eV $Å^{-1}$ on each atom.

Single crystals analysis

Suitable single crystals were placed under Paratone-N oil and transferred to an optical microscope whereby high-quality crystals were mounted onto a goniometer head and placed onto a goniometer of a single crystal diffractometer. Data for $(EDA)_2PbI_2$ were collected on a XtaLAB Synergy diffractometer which uses a micro-focus sealed X-ray tube PhotonJet (Mo K_α: $\lambda = 0.71073$ Å) as the X-ray source and a Hybrid Pixel Array Detector (HyPix). The data for $(EDA)_2PbI_2$ were then reduced in the CrysAlisPro (Rigaku) software package. Data for $(DAP)_2PbI_2$ were collected on a STOE IPDS II 2 circle diffractometer which uses a sealed X-ray tube with X-ray fibre optics (Mo K_α: $\lambda = 0.71073$ Å) for diffraction and a 34 cm diameter image plate detector. The data for $(DAP)_2PbI_2$ was reduced in the X-area software package (STOE) using a semi-empirical absorption correction, outlier rejection and frame scaling as implemented in LANA[43]. The reflection file for both compounds were then imported into Olex2[44]. A structural solution was achieved though the intrinsic phrasing method, as used in SHELXT[45], and the structure was further refined using a least squares method on F^2 as implemented in SHELXL[46]. The crystal structures were then visualized in Vesta for further structural analysis[47].

X-ray photoelectron spectroscopy

High-resolution X-ray photoelectron spectroscopy (XPS) was measured with a 140 monochromatic aluminium X-ray source (model 5600, Perkin-Elmer). All the charges were referenced to the Fermi edge and the 4*f* core level of Au (99.9999% pure) for calibration. The curves drawn on top of data in Fig. 1b,c and Supplementary Figs. 3f, 9f and 10f were guides to the eye.

XPS depth profiling

The XPS measurements were carried out on the Thermofisher ESCALAB Xi^+ system. XPS measurements were acquired using a monochromatic Al Kα source (hν = 1,486.6 eV) with a pass energy of 20 eV. The sample was transferred into the XPS chamber via a vacuum transfer module to avoid air exposure. The XPS spectra energy positions were calibrated using a cleaned Au sample. For XPS depth profiling measurements, samples were layer-by-layer sputtered off using a gas ion cluster beam with 2,000 sizes at 4 keV. The sampling point was at the centre of the sputtered crater (size: 1×1 mm^2). All the characteristic elements included in perovskites and hole transport layers are the fingerprint to distinguish each layer in multilayer stacks.

Scanning electron microscopy

A high-resolution field-emission Hitachi S-4800 scanning electron microscope was used to measure the top-view and cross-sectional images of the single-junction solar cells and tandems.

X-ray diffraction

A Rigaku Ultima III X-ray diffraction with Cu Kα radiation was used to measure and analyse the crystal structure and properties of the low-bandgap mixed Sn–Pb perovskites.

Photoluminescence characterization, imaging and quasi-Fermi level splitting analysis

Perovskite films deposited on HTL/ITO stacks using the same recipe as used for device fabrication. The phoptoluminescence (PL) and absolute PL spectra of the encapsulated samples were collected using a hyperspectral imaging system coupled to a microscope with SWIR camera (Photon etc. IMA). Excitation of the samples took place from the top surface of the perovskite layer using a 808 nm laser, under approximately 1-sun illumination condition. The absolute calibration process for the experimental set-up is described in detail elsewhere[48]. PL spectra of the samples were extracted using PHySpecV2 software. To obtain the quasi-Fermi level splitting (QFLS), the collected data were analysed using custom MatLab code, as previously reported[15].

Conductive atomic force microscope

The conductive atomic force microscope (cAFM) mappings were collected using an Asylum Research MFP3D atomic force microscope mounted on an inverted Nikon Eclipse microscope and a customized piezo-stage. All samples were loaded in a nitrogen glovebox and protected under active flowing nitrogen throughout the measurement. To extract the spatial photocurrent information, all samples were illuminated with a 455 nm LED (with intensity of ~0.8 sun) from the glass/ITO side, biased with 1.5 V, and probed with Cr/Pt-coated silicon tips (MikroMasch, 75 kHz) and a 2 nA N^{-1} tip holder. In the cAFM analysis in Supplementary Fig. 18, we grouped the current of each pixel in the cAFM images into 40 bins of equal width and defined the pixels in the first bin with current <0.1 nA as being insulating.

Photoluminescence quantum yield

The excitation source was an unfocused beam of a 442 nm c.w. diode laser. Photoluminescence was collected using an integrating sphere with a pre-calibrated fibre coupled to a spectrometer (Ocean Optics QE Pro) with an intensity of ~300 mW cm^{-2}. Photoluminescence quantum yield (PLQY) values were calculated by PLQY = PSPEx × A, where $A = 1 - PLPEx$, PS is the integrated photon count of sample emissions upon laser excitation; PEx is the integrated photon count of the excitation laser when the sample is removed from integrating sphere and PL is the integrated photon count of the excitation laser when sample is mounted in the integrating sphere and hit by the beam. A set of neutral density filters were used to vary the excitation density.

Grazing-incidence wide-angle x-ray scattering

Grazing-incidence wide-angle X-ray scattering (GIWAXS) characterization was performed at Lawrence Berkeley National Laboratory using beamline 7.3.3 of the Advanced Light Source and an energy of 10 keV. The sample to detector distance was calibrated with AgB before sample measurement. All samples were placed into a helium atmosphere with <0.03% O_2 and scattering signals collected (1 s exposure) using a 2D CCD detector (Pilatus 2 M) with a 0.172 mm by 0.172 mm pixel size. Incident angles between 0.1° and 0.222° were used for the measurement.

Time-resolved photoluminescence spectroscopy

Time-resolved photoluminescence (TRPL) measurements were performed using a Horiba Fluorolog Time Correlated Single Photon Counting system. A pulsed laser diode (504 nm, 110–140 ps pulse width, average 1.4 mW) was used as excitation sources for steady-state and transient measurements. TRPL decay curves were fitted with biexponential components to obtain a fast and a slow decay lifetime. The mean carrier lifetimes τ for the biexponential fit were calculated by the weighted average method.

Reporting summary

Further information on research design is available in the Nature Portfolio Reporting Summary linked to this article.

Data availability

All data generated or analysed during this study are included in the published article and its Supplementary Information and Source Data files. The crystallographic files for the compounds reported in this work can be found as depositions in the Cambridge Crystallographic Data Centre based on the following deposition numbers: 2269329 for $(EDA)_2PbI_2$ and 2269332 for $(DAP)_2PbI_2$. Source data are provided with this paper.

References

1. Zhao, D. et al. Efficient two-terminal all-perovskite tandem solar cells enabled by high-quality low-bandgap absorber layers. *Nat. Energy* **3**, 1093–1100 (2018).
2. Zhao, D. et al. Low-bandgap mixed tin–lead iodide perovskite absorbers with long carrier lifetimes for all-perovskite tandem solar cells. *Nat. Energy* **2**, 17018 (2017).
3. Lin, R. et al. Monolithic all-perovskite tandem solar cells with 24.8% efficiency exploiting comproportionation to suppress Sn(ii) oxidation in precursor ink. *Nat. Energy* **4**, 864–873 (2019).
4. Lin, R. et al. All-perovskite tandem solar cells with improved grain surface passivation. *Nature* **603**, 73–78 (2022).
5. Wang, C., Song, Z., Li, C., Zhao, D. & Yan, Y. Low-bandgap mixed tin-lead perovskites and their applications in all-perovskite tandem solar cells. *Adv. Funct. Mater.* **29**, 1808801 (2019).
6. Lin, R. et al. All-perovskite tandem solar cells with 3D/3D bilayer perovskite heterojunction. *Nature* **620**, 994–1000 (2023).
7. Li, Z. et al. Cost analysis of perovskite tandem photovoltaics. *Joule* **2**, 1559–1572 (2018).
8. Best research-cell efficiency Chart. *NREL* https://www.nrel.gov/pv/cell-efficiency.html (2023).
9. Green, M. A. et al. Solar cell efficiency tables (Version 61). *Prog. Photovolt. Res. Appl.* **31**, 3–16 (2023).
10. Li, C. et al. Low-bandgap mixed tin–lead iodide perovskites with reduced methylammonium for simultaneous enhancement of solar cell efficiency and stability. *Nat. Energy* **5**, 768–776 (2020).
11. Wang, Z. et al. Suppressed phase segregation for triple-junction perovskite solar cells. *Nature* **618**, 74–79 (2023).
12. Zuo, C. et al. Advances in perovskite solar cells. *Adv. Sci.* **3**, 1500324 (2016).
13. Chen, H. et al. Regulating surface potential maximizes voltage in all-perovskite tandems. *Nature* **613**, 676–681 (2023).
14. Warby, J. et al. Understanding performance limiting interfacial recombination in *pin* perovskite solar cells. *Adv. Energy Mater.* **12**, 2103567 (2022).
15. Liu, J. et al. Efficient and stable perovskite-silicon tandem solar cells through contact displacement by MgFx. *Science* **377**, 302–306 (2022).
16. Li, C. et al. Reducing saturation-current density to realize high-efficiency low-bandgap mixed tin–lead halide perovskite solar cells. *Adv. Energy Mater.* **9**, 1803135 (2019).
17. Stolterfoht, M. et al. The impact of energy alignment and interfacial recombination on the internal and external open-circuit voltage of perovskite solar cells. *Energy Environ. Sci.* **12**, 2778–2788 (2019).
18. Cao, J. et al. High-performance tin–lead mixed-perovskite solar cells with vertical compositional gradient. *Adv. Mater.* **34**, 2107729 (2022).
19. Ricciarelli, D., Meggiolaro, D., Ambrosio, F. & De Angelis, F. Instability of tin iodide perovskites: bulk p-doping versus surface tin oxidation. *ACS Energy Lett.* **5**, 2787–2795 (2020).
20. Hu, S. et al. Optimized carrier extraction at interfaces for 23.6% efficient tin–lead perovskite solar cells. *Energy Environ. Sci.* **15**, 2096–2107 (2022).
21. Jokar, E. et al. Slow surface passivation and crystal relaxation with additives to improve device performance and durability for tin-based perovskite solar cells. *Energy Environ. Sci.* **11**, 2353–2362 (2018).
22. Xiao, K. et al. All-perovskite tandem solar cells with 24.2% certified efficiency and area over 1 cm^2 using surface-anchoring zwitterionic antioxidant. *Nat. Energy* **5**, 870–880 (2020).
23. Chen, Q. et al. Unveiling roles of tin fluoride additives in high-efficiency low-bandgap mixed tin-lead perovskite solar cells. *Adv. Energy Mater.* **11**, 2101045 (2021).
24. Hu, S. et al. Synergistic surface modification of tin–lead perovskite solar cells. *Adv. Mater.* **35**, 2208320 (2023).
25. Kapil, G. et al. Tin-lead perovskite fabricated via ethylenediamine interlayer guides to the solar cell efficiency of 21.74%. *Adv. Energy Mater.* **11**, 2101069 (2021).
26. Kamarudin, M. A. et al. Suppression of charge carrier recombination in lead-free tin halide perovskite via Lewis base post-treatment. *J. Phys. Chem. Lett.* **10**, 5277–5283 (2019).
27. Lanzetta, L. et al. Degradation mechanism of hybrid tin-based perovskite solar cells and the critical role of tin (IV) iodide. *Nat. Commun.* **12**, 2853 (2021).
28. Leijtens, T., Prasanna, R., Gold-Parker, A., Toney, M. F. & McGehee, M. D. Mechanism of tin oxidation and stabilization by lead substitution in tin halide perovskites. *ACS Energy Lett.* **2**, 2159–2165 (2017).
29. Zou, Y. et al. Manipulating crystallization dynamics through chelating molecules for bright perovskite emitters. *Nat. Commun.* **12**, 4831 (2021).
30. Kurisinkal Pious, J. et al. Revealing the role of tin fluoride additive in narrow bandgap Pb-Sn perovskites for highly efficient flexible all-perovskite tandem cells. *ACS Appl. Mater. Interfaces* **15**, 10150–10157 (2023).
31. Liao, W. et al. Lead-free inverted planar formamidinium tin triiodide perovskite solar cells achieving power conversion efficiencies up to 6.22%. *Adv. Mater.* **28**, 9333–9340 (2016).
32. Krämer, U., Cotter-Howells, J. D., Charnock, J. M., Baker, A. J. M. & Smith, J. A. C. Free histidine as a metal chelator in plants that accumulate nickel. *Nature* **379**, 635–638 (1996).
33. Han, C. et al. Large-size and polarization-sensitive two-dimensional Sn perovskite single crystals. *ACS Mater. Lett.* **4**, 987–994 (2022).
34. Liu, Y. et al. Multi-inch single-crystalline perovskite membrane for high-detectivity flexible photosensors. *Nat. Commun.* **9**, 5302 (2018).
35. Taddei, M. et al. Ethylenediamine addition improves performance and suppresses phase instabilities in mixed-halide perovskites. *ACS Energy Lett.* **7**, 4265–4273 (2022).
36. Jiang, Q. et al. Surface reaction for efficient and stable inverted perovskite solar cells. *Nature* **611**, 278–283 (2022).
37. Shi, Y. et al. (3-Aminopropyl)trimethoxysilane surface passivation improves perovskite solar cell performance by reducing surface recombination velocity. *ACS Energy Lett.* **7**, 4081–4088 (2022).
38. Li, C. et al. Rational design of Lewis base molecules for stable and efficient inverted perovskite solar cells. *Science* **379**, 690–694 (2023).
39. Zhang, Y.-Y. et al. Intrinsic instability of the hybrid halide perovskite semiconductor CH3NH3PbI3. *Chin. Phys. Lett.* **35**, 036104 (2018).
40. Perdew, J. P., Burke, K. & Ernzerhof, M. Generalized gradient approximation made simple. *Phys. Rev. Lett.* **77**, 3865–3868 (1996).
41. Kresse, G. & Furthmüller, J. Efficient iterative schemes for ab initio total-energy calculations using a plane-wave basis set. *Phys. Rev. B* **54**, 11169–11186 (1996).
42. Kresse, G. & Furthmüller, J. Efficiency of ab-initio total energy calculations for metals and semiconductors using a plane-wave basis set. *Comput. Mater. Sci.* **6**, 15–50 (1996).

43. Koziskova, J., Hahn, F., Richter, J. & Kozisek, J. Comparison of different absorption corrections on the model structure of tetrakis ([mu] 2-acetato)-diaqua-di-copper (II). *Acta Chim. Slov.* **9**, 136 (2016).
44. Dolomanov, O. V., Bourhis, L. J., Gildea, R. J., Howard, J. A. K. & Puschmann, H. OLEX2: a complete structure solution, refinement and analysis program. *J. Appl. Crystallogr.* **42**, 339–341 (2009).
45. Sheldrick, G. M. SHELXT—integrated space-group and crystal-structure determination. *Acta Crystallogr. A* **71**, 3–8 (2015).
46. Sheldrick, G. M. Crystal structure refinement with SHELXL. *Acta Crystallogr. C* **71**, 3–8 (2015).
47. Momma, K. & Izumi, F. VESTA: a three-dimensional visualization system for electronic and structural analysis. *J. Appl. Crystallogr.* **41**, 653–658 (2008).
48. Delamarre, A., Lombez, L. & Guillemoles, J. F. Characterization of solar cells using electroluminescence and photoluminescence hyperspectral images. *J. Photonics Energy* **2**, 027004 (2012).

Acknowledgements

This research was made possible by US Department of Energy's Office of Energy Efficiency and Renewable Energy (EERE) under the Solar Energy Technologies Office award number DE-EE0008753, Ontario Research Fund-Research Excellence programme (ORF7-Ministry of Research and Innovation and Ontario Research Fund-Research Excellence Round 7). Work at University of Toledo was supported by Hydrogen and Fuel Cell Technologies Office award number DE-EE0008837 and by the National Science Foundation under contract number DMR-1807818. M.G.K. was supported by the Office of Naval Research (ONR) under grant N00014-20-1-2725. At King Abdullah University of Science and Technology (KAUST), this work was supported under award number OSR-2020-CRG9-4350. Single crystal diffraction experiments made use of the IMSERC Crystallography and Physical Characterization facilities at Northwestern University, which received support from the Soft and Hybrid Nanotechnology Experimental (SHyNE) resource (NSF ECCS-2025633). A.B. was supported by a fellowship through the National Defense Science and Engineering Graduate (NDSEG) Fellowship programme, sponsored by the Air Force Research Laboratory (AFRL), the Office of Naval research (ONR) and the Army Research Office (ARO). Portions of this research were conducted at beamline 7.3.3 of the Advanced Light Source, Lawrence Berkeley National Laboratory, which was supported by the Office of Science, Office of Basic Energy Sciences, of the US Department of Energy under contract number DE-AC02-05CH11231. F.J. and D.S.G. acknowledge the institutional support from the B. Seymour Rabinovitch Endowment and the state of Washington.

Author contributions

C. Li, Y.Y., B.C. and E.H.S. conceived the idea of this project. C. Li fabricated the low-bandgap and wide-bandgap subcell and assembled tandem solar cells for certification. L.C. fabricated the low-bandgap solar cells for device performance measurement and prepared single crystals and thin film samples for crystal analysis, SEM and XRD. F.J. and D.S.G. carried out cAFM and associated data analysis. B.C. helped with experimental design and data analysis. X. Wang carried out DFT calculations. E.U. and S.D.W. carried out the PL mapping and QFLS analysis. A.B. and M.G.K. carried out crystal analysis. D.L. and Z.-H.L. carried out the depth profile XPS characterization and data analysis. C. Li and Yuan Liu helped with the XPS measurement and data analysis. A.M. carried out the PLQY measurement and data analysis. C. Li, Y. Li and L.C. carried out stability tests. X. Wu, Z.F., Q.H. and T.P.R. carried out GIWAXS measurement and data analysis. L.Z., and Z.W. performed *J–V* and EQE measurements. C. Li, B.C., Z.S., Y.Y. and E.H.S. wrote and edited the paper. All the authors contributed to the discussion of the results and the final paper preparation.

Competing interests

The authors declare no competing interests.

Additional information

Supplementary information The online version contains supplementary material available at https://doi.org/10.1038/s41560-024-01613-8.

Correspondence and requests for materials should be addressed to Bin Chen, Yanfa Yan or Edward H. Sargent.

Peer review information *Nature Energy* thanks Eric Diau, Anita Ho-Baillie and Atsushi Wakamiya for their contribution to the peer review of this work.

Reprints and permissions information is available at www.nature.com/reprints.

Publisher's note Springer Nature remains neutral with regard to jurisdictional claims in published maps and institutional affiliations.

[1]Department of Electrical and Computer Engineering, University of Toronto, Toronto, Ontario, Canada. [2]Department of Chemistry, Northwestern University, Evanston, IL, USA. [3]Department of Physics and Astronomy, University of Toledo, Toledo, OH, USA. [4]Department of Chemistry, University of Washington, Seattle, WA, USA. [5]King Abdullah University of Science and Technology (KAUST), KAUST Solar Center (KSC), Physical Sciences and Engineering Division (PSE), Thuwal, Kingdom of Saudi Arabia. [6]Center for Materials and Sensors Characterization, The University of Toledo, Toledo, OH, USA. [7]Materials Sciences Division, Lawrence Berkeley National Laboratory, Berkeley, CA, USA. [8]Polymer Science and Engineering Department, University of Massachusetts Amherst, Amherst, MA, USA. [9]Department of Materials Science and Engineering, University of Toronto, Toronto, Ontario, Canada. [10]Advanced Membranes and Porous Materials Center, Physical Science and Engineering Division, KAUST, Thuwal, Saudi Arabia. [11]School of Materials Science and Engineering, Georgia Institute of Technology, Atlanta, GA, USA. [12]Advanced Institute for Materials Research (WPI-AIMR), Tohoku University, 2-1-1 Katahira, Aoba, Senda, Japan. [13]Department of Electrical and Computer Engineering, Northwestern University, Evanston, IL, USA. [14]These authors contributed equally: Chongwen Li, Lei Chen, Fangyuan Jiang, Zhaoning Song. ✉e-mail: bin.chen@northwestern.edu; yanfa.yan@utoledo.edu; ted.sargent@northwestern.edu

nature portfolio

Corresponding author(s): Edward Sargent

Solar Cells Reporting Summary

Nature Portfolio wishes to improve the reproducibility of the work that we publish. This form is intended for publication with all accepted papers reporting the characterization of photovoltaic devices and provides structure for consistency and transparency in reporting. Some list items might not apply to an individual manuscript, but all fields must be completed for clarity.

For further information on Nature Research policies, including our data availability policy, see Authors & Referees.

Experimental design

Please check the following details are reported in the manuscript, and provide a brief description or explanation where applicable.

1. Dimensions

Area of the tested solar cells	☒ Yes ☐ No	Solar Cell Characterizations section: 0.049 cm2 for small-area and 1.05 cm2 for large-area devices *Explain why this information is not reported/not relevant.*
Method used to determine the device area	☒ Yes ☐ No	Solar Cell Characterizations section: The aperture shade mask (0.049 cm2 for small-area and 1.05 cm2 for large-area devices) determined the active area of the solar cell *Explain why this information is not reported/not relevant.*

2. Current-voltage characterization

Current density-voltage (J-V) plots in both forward and backward direction	☒ Yes ☐ No	Fig. 3a, 4c, 4e and Supplementary Fig. 26, Supplementary Fig. 31 and Supplementary Fig. 32
Voltage scan conditions	☒ Yes ☐ No	Solar Cell Characterizations section: a scanning rate of 100 mV/s (voltage step of 10 mV and delay time of 100 ms) *Explain why this information is not reported/not relevant.*
Test environment	☒ Yes ☐ No	Solar Cell Characterizations section: J-V curves measurement with a scanning rate of 100 mV/s (voltage step of 10 mV and delay time of 100 ms) and stabilized power output (SPO) measurement were conducted in nitrogen atmosphere without cooling; The humidity of the measurement environment ranged from 40 to 60% *Explain why this information is not reported/not relevant.*
Protocol for preconditioning of the device before its characterization	☐ Yes ☒ No	*Provide a description of the protocol.* We don't set preconditioning for before characterization
Stability of the J-V characteristic	☒ Yes ☐ No	Solar Cell Characterizations section: Maximum power point (MPP) tracking measurements were conducted using a Candlelight stability test station in the air and under a white light LED solar simulator with simulated AM 1.5G spectrum. The humidity of the measurement environment ranged from 40 to 60% *Explain why this information is not reported/not relevant.*

3. Hysteresis or any other unusual behaviour

Description of the unusual behaviour observed during the characterization	☐ Yes ☒ No	*Provide a description of hysteresis or any other unusual behaviour observed during the characterization.* We observed negligible hysteresis
Related experimental data	☒ Yes ☐ No	Fig. 3a, 4c, 4e and Supplementary Fig. 26, Supplementary Fig. 31 and Supplementary Fig. 32 *Explain why this information is not reported/not relevant.*

4. Efficiency

External quantum efficiency (EQE) or incident photons to current efficiency (IPCE)	☒ Yes ☐ No	Fig. 4d *Explain why this information is not reported/not relevant.*

A comparison between the integrated response under the standard reference spectrum and the response measure under the simulator

☒ Yes
☐ No

Certified results shown in Fig. 4 g and Fig. 4e

Explain why this information is not reported/not relevant.

For tandem solar cells, the bias illumination and bias voltage used for each subcell

☒ Yes
☐ No

Solar Cell Characterizations section: To extract the spatial photocurrent information, all samples were illuminated with a 455 nm LED (with intensity of ~ 0.8 sun) from the glass/ITO side, biased with 1.5 V, and probed with Cr/Pt-coated silicon tips (MikroMasch, 75 kHz) and a 2 nA/N tip holder

Explain why this information is not reported/not relevant.

5. Calibration

Light source and reference cell or sensor used for the characterization

☒ Yes
☐ No

Solar Cell Characterizations section: A standard Si solar cell was used as the reference for calibration

Explain why this information is not reported/not relevant.

Confirmation that the reference cell was calibrated and certified

☒ Yes
☐ No

Solar Cell Characterizations section: A standard Si solar cell was used as the reference for calibration

Explain why this information is not reported/not relevant.

Calculation of spectral mismatch between the reference cell and the devices under test

☒ Yes
☐ No

The spectral mismatch is negligible as the difference between the short-circuit current density measured by our solar simulator and the integrated current density measured by EQE was insignificant

Explain why this information is not reported/not relevant.

6. Mask/aperture

Size of the mask/aperture used during testing

☒ Yes
☐ No

Solar Cell Characterizations section: The aperture shade mask (0.049 cm2 for small-area and 1.05 cm2 for large-area devices) determined the active area of the solar cell

Explain why this information is not reported/not relevant.

Variation of the measured short-circuit current density with the mask/aperture area

☒ Yes
☐ No

Fig. 3b and Supplementary Fig. 24 and Supplementary Fig. 27

Explain why this information is not reported/not relevant.

7. Performance certification

Identity of the independent certification laboratory that confirmed the photovoltaic performance

☒ Yes
☐ No

Fig. 4e, J–V scans from Japan electrical safety & environment technology laboratories (JET) delivered a PCE of 27.4 % (Fig. 4e, Supplementary Fig. 31 and Note 5)

Explain why this information is not reported/not relevant.

A copy of any certificate(s)

☒ Yes
☐ No

Supplementary Fig. 22

Explain why this information is not reported/not relevant.

8. Statistics

Number of solar cells tested

☒ Yes
☐ No

Fig. 2h, Fig. 3b, Supplementary Fig. 7, Supplementary Fig. 19, Supplementary Fig. 27, Supplementary Fig. 29 and their captions

Explain why this information is not reported/not relevant.

Statistical analysis of the device performance

☒ Yes
☐ No

Fig. 2h, Fig. 3b, Supplementary Fig. 7, Supplementary Fig. 19, Supplementary Fig. 27 and Supplementary Fig. 29

Explain why this information is not reported/not relevant.

9. Long-term stability analysis

Type of analysis, bias conditions and environmental conditions

☒ Yes
☐ No

Fig. 3d, 3e, Fig. 4f and the Solar Cell Characterizations section

Explain why this information is not reported/not relevant.